Reconstructing longitudinal strain pulses using time-resolved x-ray diffraction

Y. Gao, Z. Chen, Z. Bond, A. Loether, L. E. Howard, S. LeMar, S. White, A. Watts, B. C. Walker, and M. F. DeCamp

Phys. Rev. B **88**, 014302 — Published 8 July 2013

DOI: 10.1103/PhysRevB.88.014302

Reconstructing longitudinal strain pulses using time-resolved x-ray diffraction

Y. Gao, Z. Chen, Z. Bond, A. Loether, L.E. Howard, S. LeMar, S. White, A. Watts, B.C. Walker, and M. F. DeCamp
Department of Physics and Astronomy, University of Delaware, Newark DE 19716
(Dated: June 5, 2013)

Time-resolved x-ray diffraction is a very powerful tool for visualizing transient one-dimensional crystalline strains, ranging from crystal growth to shockwave production. In this work, we use picosecond x-ray diffraction to visualize transient strain formation from nanometer scaled laser excited gold films into crystalline substrates. We show that there is a direct correspondence between the measured time-resolved x-ray diffraction pattern and the transient acoustic wave, providing a straightforward method to make a reconstruction of the transient strain. In addition, we discuss real-world experimental constraints that place limits on the validity of the reconstructed transient acoustic wave.

I. INTRODUCTION

Understanding the dynamics driven by intense optical radiation is of fundamental importance to a diverse set of fields, ranging from structural phase transitions[1–4] to biophysics[5,6]. In solid state systems, for example, upon ultrafast optical excitation, the resultant impulsive surface heating can produce a transient longitudinal acoustic pulse. The central wavelength of this strain pulse can be as small as a few nanometers, providing a method to directly image of nanometer scale structures and biomaterials[7,8]. Direct comparisons of theoretical models with experiments can lead to an understanding of electron-phonon interactions and thermal properties of materials[1,9–16].

Experimental studies of ultrafast dynamics are often based upon stroboscopic pump-probe techniques, whereby a fast optical pump pulse excites the material, and a separate fast probe pulse measures the induced distortion. While very successful, traditional optical pump-probe spectroscopies can only measure changes in either the material's dielectric constant and/or electronic resonances, making an atomic scale reconstruction of the material strain difficult. In contrast, due to its short wavelength, hard x-ray radiation can directly probe atomic scale structure. Integrating stroboscopic pump-probe techniques with classic x-ray Bragg diffraction has introduced a new spectroscopic tool for measuring transient structural deformations on the atomic scale, time-resolved x-ray diffraction (TRXRD).

With the development of high-brightness, short pulse, hard x-ray sources in the last 25 years, TRXRD has rapidly grown to study a whole range of laser initiated structural dynamics[1,3,5,11,12,16–23]. Like traditional optical pump-probe techniques, TRXRD typically utilizes an intense optical pump pulse to rapidly initiate structural change through the rapid heating of the material. Following photo excitation, a short x-ray pulse diffracts from the excited sample to take a quasi-instantaneous image of the atomic scale structure. The ultrafast dynamics are revealed by adjusting the time-delay between the optical pulse and the diffracted x-ray beam, creating a series of atomic scale structural images of the excited system.

In this work, we use TRXRD to study the formation of ultrafast longitudinal acoustic pulses in crystalline systems. Transient acoustic pulse are generated by the ultrafast excitation of thin gold films on a crystalline Germanium substrate. Previously we demonstrated that the maximum wave-vector of the photogenerated acoustic pulse is determined by the film thickness[24]. Here we extend that work by studying the acoustic pulse formation in a variety of film thicknesses and directly comparing the TRXRD patterns to numerical dynamical diffraction calculations. In addition, we show that, in principle, it is possible to make a one-to-one correspondence between the experimental TRXRD patterns and the spatio-temporal shape of a longitudinal pulse.

II. TIME-RESOLVED X-RAY DIFFRACTION : EXPERIMENT

For time-domain x-ray diffraction studies we utilize a table-top picosecond x-ray source to measure the ultrafast lattice dynamics induced by intense optical radiation on photo excited metallic films on a crystalline substrate. By modifying the thickness of the metallic film we can choose the maximum acoustic wave-vector that is generated. In the following section, we describe the experimental setup in detail and the resulting experimental measurements of the acoustic pulse generation.

A. Experimental Setup

To measure the spatio-temporal shape of a ultrafast longitudinal acoustic pulse, we utilize a home-built femtosecond laser-plasma x-ray source (see figure 1). The optical pump and hard x-ray probe beams were derived from a 1 kHz Ti:sapphire chirped pulsed regenerative amplifier (Spectra Physics, Spitfire). Prior to final pulse compression, two optical elements were added to the amplifier system; an additional Pockel's cell providing pre-pulse contrast of greater than 10^5:1 and an optical beam splitter, such that $\sim$0.3 mJ of the chirped optical light was used as a seed for a home-built cryogenically cooled multi-pass amplifier. The residual chirped amplified beam was compressed to $\sim$40 fs, and was used for

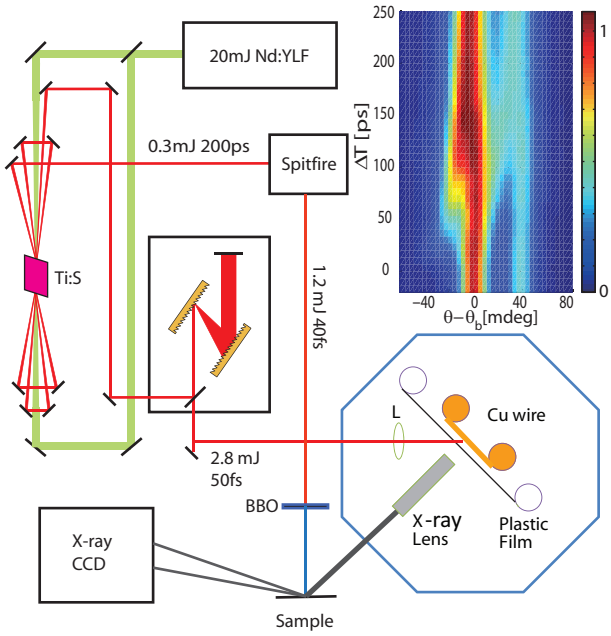

FIG. 1. Experimental geometry for the laser-pump/x-ray probe setup. Inset: Prototypical TRXRD of laser excited of an uncoated Ge (111) crystal.

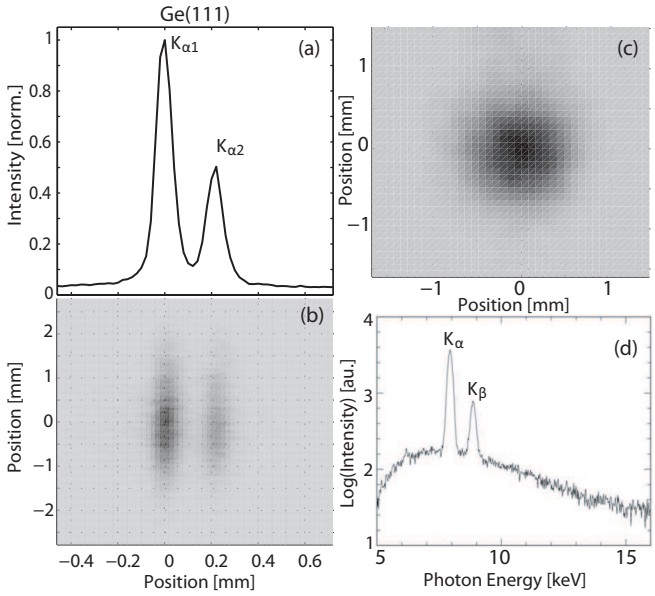

FIG. 2. (a) Vertical summation of (b) Measured x-ray diffraction from Ge (111) single crystal. (c) Measured x-ray focus from the polycapillary optic (d) Typical hard x-ray spectrum from the laser plasma source.

the optical excitation.

The picosecond x-ray probe pulse was generated by the compressed output of the multi-pass amplifier focused onto a solid copper target. The cryogenically cooled multi-pass Ti:sapphire amplifier was pumped by 1kHz, 20 mJ, frequency doubled Nd:YLF Q-switched laser. After compression, the four-pass amplifier achieved a final pulse energy of ∼2.9 mJ and a pulse length of ∼50 fs. The generation of the x-ray pulse was achieved by the focusing of the optical pulse using an f-#15 optic, onto a moving copper wire housed in a lead lined vacuum chamber held at a base pressure of less than 100 mTorr. To shield the optical elements from the copper debris generated in the laser-plasma formation, a thin (∼25 μm) moving cellophane sheet was placed in front of the copper target. X-ray spectral analysis of generated x-ray yield was performed by a single channel silicon x-ray spectrometer (Amptek X-123), and revealed that the total integrated hard x-ray flux was in excess of 10^{11} hard x-ray photons per second, of which ∼30% was in the copper k-alpha lines (see figure 2d). Previously published work done on the THz emission from this target, demonstrated that the emitted radiation is on order of 1 ps[25], consistent with similar x-ray sources[3].

To increase the x-ray flux at the sample, a polycapillary x-ray optic (XOS systems) with an input focal length of 25 mm and output focal length of 45 cm collected the hard x-ray photons and focused them onto the target of interest. The resultant quasi-collimated x-ray beam (angular divergence of ∼0.25°) produced a ∼1 mm diameter focus at the sample consisting of a hard-x-ray photon flux of 10^6 photons/sec (see figure 2c). The lens introduced minimal change in the optical path length, thereby producing negligible temporal dispersion on the x-ray pulse. To increase the angular resolution of the diffraction experiment, 100 μm wide tungsten slits were inserted prior to the sample.

Following Bragg diffraction from the sample of interest, the x-ray flux was collected by a free standing, cryogenically cooled, direct detection x-ray CCD camera (Princeton Instruments) placed approximately 50 cm from the sample. The combination of the tungsten slits, CCD pixel size, and distance from the sample resulted in an angular resolution of ∼5 mdeg , sufficient to accurately measure the copper k-alpha lines (see figure 2a, b). Angular calibration of the camera was determined by the measured location of the spin split copper k-alpha lines from an unexcited Ge (111) crystal. Several images (>4) were taken at each time delay to remove the effects of long term drift and changes in the optical intensity at the copper wire due to the moving cellophane sheet.

Experiments were performed on a series of gold coated Ge (111) crystals, with film thicknesses ranging from 50 nm to 270 nm. 50±5 nm and 100±10 nm gold films were grown on 0.5 mm thick undoped Ge (111) substrates by magnetron-sputtering. ∼270 nm Gold film was deposited onto a similar Ge substrate by utilizing $KAuCl_4$ and hydrofluoric acid (HF) to grow a "quasi-single-crystalline" gold film[26]. The thickness of this film was determined by SEM cross section viewing (see figure 3b). The samples were excited by the ultrafast laser after frequency doubling to 400 nm in a 100 μm thick β-barium borate crystal. The optical sample was excited by both the residual 800 nm and 400 nm light resulting in a total incident

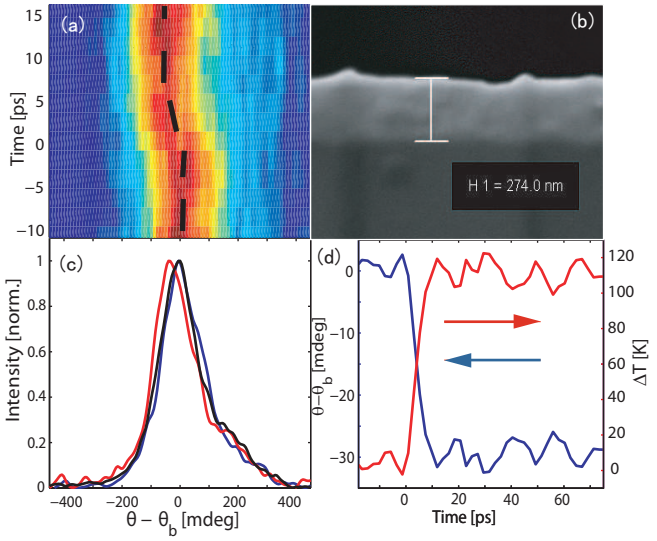

FIG. 3. (a) TRXRD pattern of Au (111) from the 270 nm gold film. Dashed line is the location of the centroid of the measured diffraction peak. (Note: the hyperfine-spin splitting of the copper k_α radiation cannot be observed due to the natural width of the Au (111) diffraction peak.) (b) SEM of cross section of gold film. (c) Measured x-ray diffraction rocking curves at a laser/x-ray time delay of -15 ps (blue), +20 ps (red) and +650 ps (black). (d) Time-resolved angular shift (blue) of Au (111) and the inferred temperature rise (red).

optical fluence of ∼10 mJ/cm^2. As the 800 and 400 nm light has approximately same optical absorption depth (∼15 nm), we assume the photo-initiated carrier dynamics, and therefore the strain dynamics, are identical for both radiation fields. Additional measurements pumping solely with 800nm radiation (not shown) did not make significant changes to the diffraction patterns. Since all these films are significantly thicker than the optical penetration depth, the resulting strain in all the three Ge substrates are due entirely to the dynamics in the gold film. To determine the temporal and spatial overlap of all three samples, a TRXRD experiment from an 800 nm pumped uncoated Ge (111) crystal was performed (see figure 1 inset).

B. Experimental Results

Laser induced carrier dynamics in the gold film were characterized by a TRXRD experiment. In particular the temporal evolution of the Au (111) diffraction peak from the 270 nm gold film was measured (see figure 3). Upon ultrafast excitation, a shift in the diffraction peak to lower angles is clearly observed. Fitting the x-ray diffraction peaks to a series of gaussian curves, we determined that the gold lattice has expanded by ∼0.1% in under 10 ps, consistent with previously published results[16]. Using the accepted value of the lattice expansion coefficient of bulk gold (1.4×10^{-5} K^{-1}), the resulting lattice expansion indicates that the gold film has increased in temperature by ∼100 K. At intermediate time delays (10 ps< ΔT <100 ps), the location of the gold diffraction peak changes minimally, and by 650 ps, the peak has returned to its pre-pumped position indicating the cooling process takes on order of 500 ps. If we assume the diffusion of hot electrons is much faster than the electron-phonon coupling time of the system and that the laser-generated strain is spatially homogeneous in the film, an optical fluence of 10 $\frac{mJ}{cm^2}$ will produce a local temperature rise in the gold film of ∼100 K, consistent with the measured angular shift of Au (111) peak.

Following the Gold film experiments, we proceeded to measure the TRXRD patterns of the photoexcited gold coated Ge (111) crystals. In Figure 4, differential diffraction intensity of x-ray Bragg diffraction patterns from Ge (111) substrates are shown. The x-ray diffraction intensity is normalized by the intensity of the Cu-Kα1 diffraction peak (angular location θ_b). To reduce the pixel noise, the rocking curves, the data is convolved with a two-dimensional Gaussian function of comprised of a temporal and angular widths of 5 ps and 7 mdeg respectively. For comparison, we also include the differential diffraction intensity of an uncoated Ge (111) crystal (figure 4a).

Upon inspection, there are several distinct differences between the coated and uncoated samples. The uncoated sample demonstrates an almost universal increase in diffraction efficiency for all angles (indicating the generation of additional sideband components) as well as a global peak shift to lower diffraction angles (which is indicative of 'static' surface heating). However, at early time delays, ΔT < 50 ps, each of the coated samples display a reduction in diffraction intensity on the negative sidebands, indicating a destructive interference between the strained lattice and the unstrained lattice. The dip in diffraction efficiency is consistent with the generation of a localized longitudinal acoustic pulse in the Ge substrate has the compression layer leading the expansion layer[24]. The uncoated Ge sample doesn't show this phenomena due to the rapid electron plasma diffusion in the Ge crystal, which generates a dramatically spatially broadened acoustic pulse that propagates into the crystalline substrate[15,27]. In addition, we observe a sample dependent time delay in the dip of the diffraction efficiency. This temporal shift is likely due to the acoustic wave propagation through the varying thickness gold films prior to the transmission to the Ge substrate.

For both the 50 nm and 100 nm gold film coated Ge crystals, positive diffraction sidebands are observed immediately after laser excitation, where the maximum angular shifts appear at ∼30 ps and ∼53 ps respectively. Following the positive sidebands, the maximum negative angular shift from 50 nm gold film, ∼50 mdeg, is observed at ∼66 ps while negative sidebands up to ∼25 mdeg are apparent at ∼83 ps for the 100 nm film. The temporal shift between the generation of positive and negative sidebands demonstrates that the strain in the Ge substrate is a bipolar acoustic pulse[18,24]. In addition, the differ-

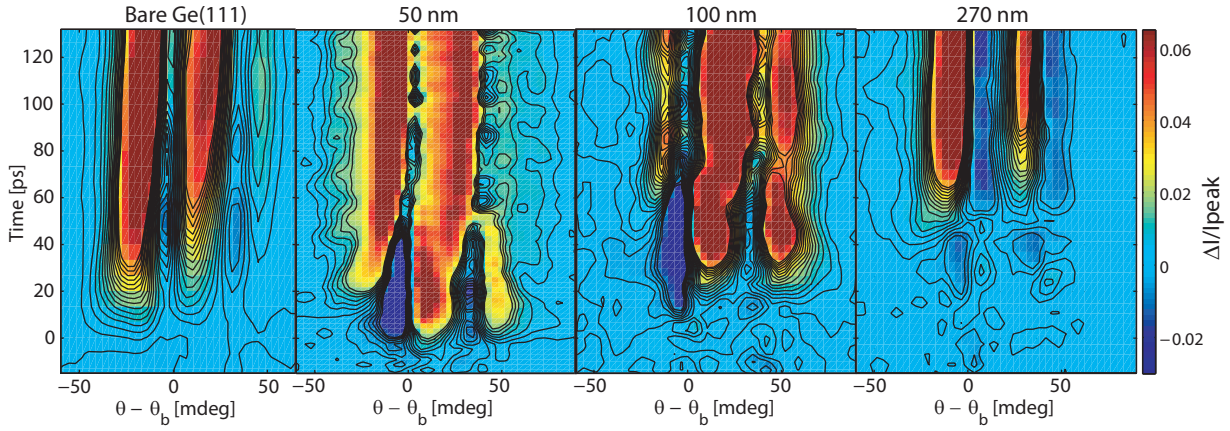

FIG. 4. Differential TRXRD measurements of gold coated Ge(111) crystals of various thicknesses. Left to right uncoated Ge, 50 nm, 100 nm, and 270 nm gold film. θ_b represents the Bragg angle for the undisturbed Ge(111) peak upon Cu$k_{\alpha 1}$ radiation.

ent maximum angular shifts of two samples, is consistent with the generation of the maximum wave-vector generation being determined by the thickness of the metallic film.

While the sidebands on the uncoated sample slowly (>100 ps) return to their equilibrium positions, the 50 and 100 nm samples exhibit clear temporal modulations in the diffraction intensity on both the positive and negative angles. The temporal oscillations are π phase shifted across the diffraction peak. In the 50 nm sample, temporal oscillations with periods up to ∼20 ps are clearly seen, while in the 100 nm sample oscillation periods of up to 40 ps are visible. Between the two diffraction peaks, a temporal beat pattern is also observed due to the combination of positive and negative sidebands from the Kα1 and Kα2 peaks respectively. Following the temporal oscillations, the 50 and 100 nm films show additional sidebands on the positive diffraction angles that slowly recover over a period of ∼1 ns. These observations are consistent with a transient bipolar acoustic pulse traveling from the metallic film into the crystalline substrate.

For the 270 nm coated sample, a diffraction peak shift without any discernible temporal oscillation is seen. This indicates that the oscillation period is too long to be distinguished from the cooling process of the gold film. However, we still observe a rapid positive shift in the peak position at early time delays (<50 ps), indicating the existence of a transient pressure front from the film being exerted onto the Ge substrate.

III. STRAIN PULSE RECONSTRUCTION

While cursory inspection of the TRXRD patterns indicate the generation of a bipolar acoustic pulse, to retrieve the spatio-temporal profile of the strain front we need to directly compare the data with simulated strains. This process is performed by the direct comparisons between the data and numerically reconstructed TRXRD patterns for a given strain profile. However, this reconstruction is meaningless unless it is known that the measured TRXRD pattern is unique to the strain. Below we will demonstrate that, in principle, it is possible to uniquely reconstruct a one-dimensional longitudinal strain pulse from the time-resolved x-ray diffraction patterns. We will also discuss the experimental limitations of this reconstruction and the implications for time-resolved x-ray Bragg diffraction.

A. One-Dimensional X-ray Diffraction

In a x-ray Bragg diffraction pattern, the magnitude and location of scattered x-ray photons is the given by the spatial Fourier transform of the crystalline lattice. In particular, the structure factor of a crystal is represented by:

$$F(\vec{q}) = D \int f(\vec{r}) e^{-i\vec{q}\cdot\vec{r}} dV \tag{1}$$

where D is a proportionality constant, $\vec{q} = \vec{k_h} - \vec{k_o}$ is the difference between the incoming ($\vec{k_o}$) and outgoing ($\vec{k_h}$) x-ray photons, $F(\vec{q})$ is the crystalline structure factor in the direction $\vec{q}$, and $f(\vec{r})$ are the location of the lattice planes[28,29]. For crystalline materials, the locations of lattice planes can be represented as a Fourier sum of the different structure factors:

$$f(\vec{r}) = \sum_m F_m e^{i\vec{G}_m\cdot\vec{r}} \tag{2}$$

where $\vec{G}_m$ is the reciprocal lattice vector of the m^{th} diffraction plane.

In the vicinity of a specific x-ray diffraction peak, $H = (hkl)$ and ($\vec{G}_H \cdot \vec{r} >> \vec{G}_{m\neq H} \cdot \vec{r}$), $f(\vec{r})$ is a periodic function with a lattice spacing of $d = \frac{2\pi}{|G|}$. The location of the diffraction peak is dictated by Bragg's Law ($2d\sin\theta = \lambda$) or the Laue Equation ($\vec{k_o} + \vec{G} = \vec{k_h}$).

However as x-ray detectors are only sensitive to the intensity of the incoming x-ray radiation, an x-ray diffraction pattern will only reveal the magnitude of $F(\vec{q})$, losing the spatial phase information associated with the crystal lattice.

In crystals that possess strain, for example, a traditional x-ray Bragg diffraction curve will show diffraction sidebands associated with the applied strain. A cursory inspection of Bragg's law would imply that the location of the diffraction sidebands are dictated solely by the magnitude of the strain. However, this is not necessarily the case. In particular, in the case of a one-dimensional longitudinal strain, the strain profile can be represented as a Fourier sum of discrete phonon wave-vectors along the z-direction:

$$\eta(z) = \sum_n A(q_n) e^{i(q_n z + \phi_n)} \tag{3}$$

where $A(q_n)$ is the amplitude of a particular momentum component (q_n), and ϕ_n is the relative spatial phase of a particular acoustic wave-vector. This strain modifies the locations of the atomic planes:

$$f'(\vec{r}) = (1 + \eta(z)) f(\vec{r}) \tag{4}$$

In the vicinity of an x-ray diffraction peak, we can combine equations 3 and 4:

$$f'(\vec{r}) \sim F_H e^{i\vec{G}_H \cdot \vec{r}} \left(1 + \sum_n A(q_n) e^{i(q_n z + \phi_n)} \right) \tag{5}$$

The resulting x-ray Bragg diffraction will be therefore be the superposition of an x-ray diffraction pattern of a unstrained crystal with a strained crystal possessing the added phonon acoustic wave-vectors.

If we represent the crystalline strain as a series of momentum components added to the crystalline lattice, $\vec{G} \rightarrow \vec{G} \pm \vec{q}$, the Laue equation will be modified to $\vec{k}_o + \vec{G} \pm \vec{q}_m = \vec{k}_H$, where $\vec{q}_m$ represent the additional phonon wave-vectors. For symmetric x-ray reflections, a specific wave-vector can be identified by the angular location of the diffraction sideband[19,30]:

$$q_m = \frac{\Delta\theta_m |G|}{\tan\theta_b} \tag{6}$$

where $\Delta\theta_m$ is the angular deviation from the Bragg condition.

This superposition can be demonstrated by numerically calculating x-ray rocking curve of a strained crystal. To model the diffraction pattern of a longitudinal strained crystal, we use the diffraction algorithm developed by Wie et al[31]. This algorithm numerically solves the Takagi-Taupin equations[32–34] governing dynamical x-ray diffraction for perfect crystals with a strained surface.

In figure 5 we calculate the x-ray Bragg diffraction pattern of a crystal with a one-dimensional sinusoidal longitudinal strain with a wave vector of $10^{-3}|G|$ and amplitude of $\frac{\Delta d}{d} = 5 \times 10^{-4}$ inside a crystalline substrate.

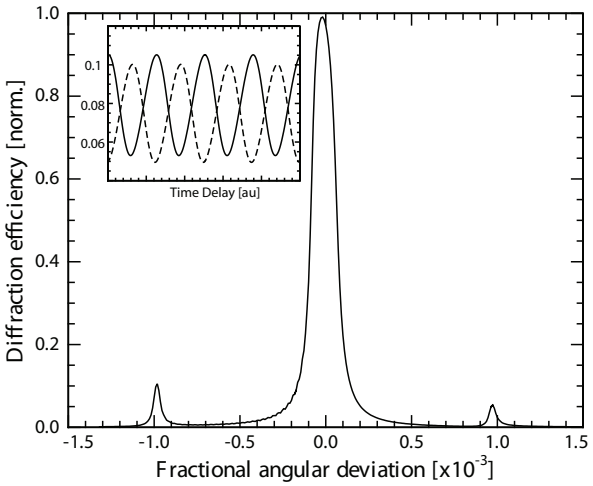

FIG. 5. Simulated Bragg diffraction pattern of a traveling one-dimensional longitudinal strain wave. Inset: Time-dependent intensity modulation of negative (solid) and positive (dashed) sidebands.

As expected, the resulting diffraction pattern has sidebands on either side of the fundamental Bragg peak, due to the interference between the scattering from the unstrained crystalline lattice and the strained lattice. The location of these sidebands is dictated by the acoustic wave-vector, while the amplitude is determined by both the strain amplitude and the spatial phase of the strain wave. For propagating strain profiles, the sideband oscillates according to the acoustic frequency of the wave, however the measured temporal phase of the oscillations is dependent on which sideband is measured (see figure 5 inset).

B. Time-resolved x-ray diffraction

While a single x-ray rocking curve can measure the presence of an acoustic disturbance, due to the inability to measure both the phase and amplitude of each momentum component simultaneously, a one-dimensional rocking curve analysis of a single Bragg peak cannot determine the exact location and shape of the strain within the crystal. In particular, the diffraction intensity depends on both the the amplitude of a particular acoustic wave-vector ($A(q)$) as well as the phase (ϕ_m) of the acoustic mode. Several computational methods have been developed which can calculate the x-ray rocking curve due to a known the crystalline structure profile[31,35,36], however, a direct inversion from a single x-ray diffraction peak is quite difficult. In cases where the one-dimensional strain is both static and monotonic, it has been shown that the diffraction pattern can be uniquely inverted to reveal the strain profile[37]. However, in transient strain pulses, typically neither of these conditions are met, making a direct inversion from a single x-ray rocking curve impossible. However, a time-resolved x-ray diffraction pattern can

provide enough information to reconstruct the spatio-temporal shape of the transient acoustic pulse.

In general, a longitudinal acoustic pulse can be represented as a Fourier sum of acoustic waves of differing wave-vectors and frequencies:

$$\eta(z,t) = \sum_n A(q_n,\omega_n)e^{i(q_n z-\omega_n t+\phi_n)} \tag{7}$$

where $\eta(z,t)$ is the longitudinal strain as a function of depth and time, and q_n, ω_n, $A(q_n,\omega_n)$, and ϕ_n are the wave-vector, frequency, amplitude, and phase of the nth mode of the acoustic excitation respectively. At first glance, this expression would appear to imply that a three-dimensional measurement is required to uniquely reconstruct the acoustic pulse. However, utilizing the material properties the dimensionality strain profile can be reduced, such that the two-dimensional TRXRD pattern can be inverted to reveal the strain profile.

A transient strain pulse can be broken up into two distinct constituent components; a propagating wave and a 'static' strain. Here we define the static strain as one where the phonon wave-vector evolves on a timescale much slower than the ratio of the x-ray absorption depth to the sound velocity. In the vicinity of a strong x-ray reflection, equation 5 can be rewritten as:

$$f'(\vec{r},t) = F_H e^{i\vec{G}\cdot\vec{r}}\left(1+\sum_n A(q_n,\omega_n)e^{i(q_n z-\omega_n t+\phi_n)}+\sum_m A(q_m)e^{i(q_m z+\phi_m)}\right) \tag{8}$$

The resultant x-ray diffraction pattern will then be the superposition of the diffraction pattern from a perfect crystal, the traveling acoustic wave, and the static strain.

Like before, the traveling wave component as currently written in equation 7, is dependent on three seemingly independent variables (q_n, ω_n, and ϕ_n). As acoustic pulses are determined by elasticity of the material, however, the frequency of a particular phonon mode is governed by the acoustic dispersion relation, $\omega_q = |C(q)|$. In cases where the acoustic frequency is low, the acoustic dispersion relation is equal to $\omega_q = v_s|q|$. Given this constraint, the traveling wave can be represented as:

$$\eta(z,t) = \sum A(q_n)e^{i(q_n z+\phi_n)}e^{i|q_n|v_s t} \tag{9}$$

This relationship now has two unknown quantities, the spectral phase ϕ_n and spectral power ($A(q_n)$) of the acoustic pulse. Although equation 9 is only valid for low frequency excitations, provided the dispersion relationship is known for the material in question, a similar equation can be derived relating the strain to only the spectral phase and spectral power. Taking this time-resolved spatial strain into account, the spatial locations of the lattice planes for the traveling wave is represented by:

$$f'(\vec{r},t) = F_H e^{i\vec{G}\cdot\vec{r}}\left(1+\sum_n A(q_n)e^{i(q_n z+\phi_n)}e^{i|q_n|v_s t}\right) \tag{10}$$

The Fourier transform of this spatial function reveals that the diffraction peak will possess oscillating side-bands associated with the additional acoustic wave-vectors. As a consequence, a standard x-ray rocking curve analysis will possess diffraction sidebands associated with the interference between the strained and unstrained crystals. In addition, these side-bands will now oscillate in time with a frequency ω_n[1,18,19,38].

For example, if the shape of the traveling wave is sinusoidal, there will be two x-ray diffraction sidebands oscillating at a frequency of the acoustic mode (see figure 5 inset), with a temporal phase related to the shape of the traveling strain wave. As one travel farther from the Bragg diffraction peak, and thus probing larger phonon wave-vectors, the frequency of these oscillations increase per the acoustic dispersion relationship. If the relative timing between the pump and x-ray probe is known with enough accuracy, a numerical Fourier transform of this oscillation can reveal both the power and phase of a particular coherent phonon mode. Therefore, transforming the entire 2D TRXRD pattern will then reveal the entire power spectrum and the spectral phase of the acoustic pulse, making a unique reconstruction possible.

A simulated time-resolved x-ray Bragg diffraction of an impulsively strained, single crystal is shown in Figure 6. In this simulation, a transient bipolar acoustic pulse, whose central wave-vector is larger than the x-ray extinction/absorption depth, in a crystal that is much thicker than the x-ray absorption depth. Upon a cursory inspection of the TRXRD pattern, several things are clear: there are temporal oscillations in the diffraction intensity as a function of time and diffraction angle, the oscillations have a finite lifetime, and the phase of oscillations on either side of the Bragg peak are inverted. Physically the lifetime is proportional to the ratio of the x-ray absorption depth and the sound velocity. In many semi-conductor systems, the hard x-ray absorption depth is typically larger than 1 micron, therefore for low order diffraction conditions can have greater than 10,000 discrete acoustic modes.

Figure 7 shows the spectral amplitude and phase of three different acoustic pulses: an acoustic pulse model via the formalism of Thomsen *et al.*[10], symmetric bipolar pulse, and a 100 nm bipolar square wave. For direct

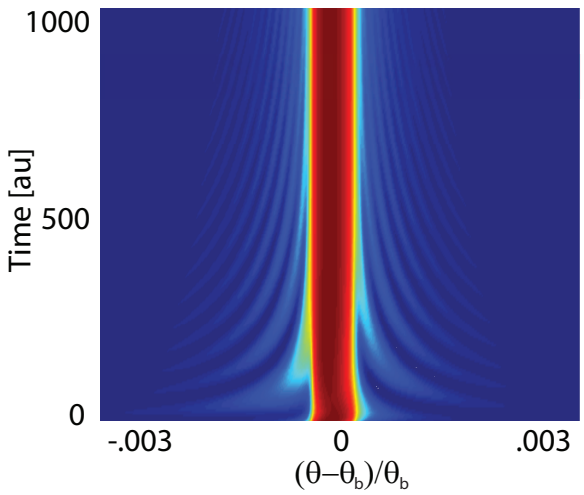

FIG. 6. TRXRD simulation for a bipolar longitudinal acoustic strain pulse in an arbitrary thick single crystal.

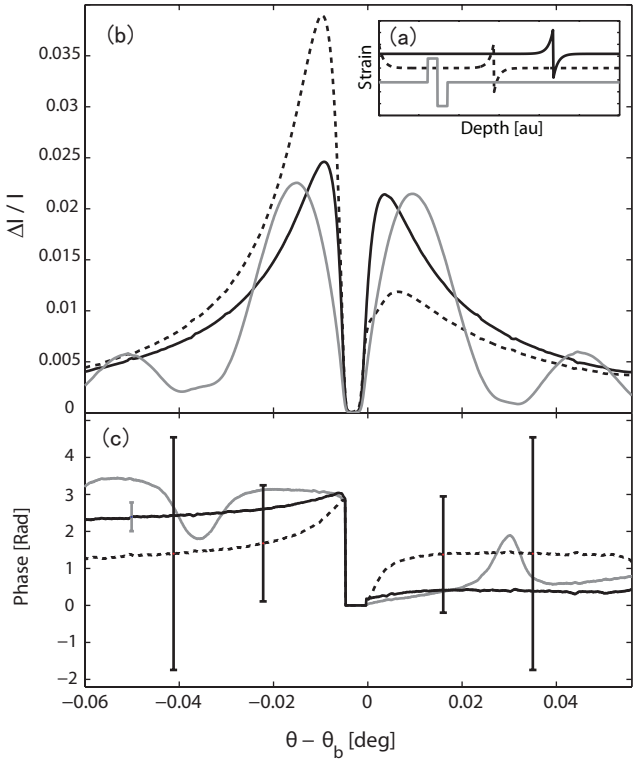

FIG. 7. (a) Simulated strain profiles for the full Thomsen model (dashed), Thomsen phonon only (black) and square (gray). Each curve is offset for clarity. (b) Retrieved spectral amplitude and (c) initial phase of the phonon oscillation. The red error bars represent phase retrieval error due to a 100 ps x-ray pulse. The blue error bar represents phase error associated with a 5ps x-ray pulse.

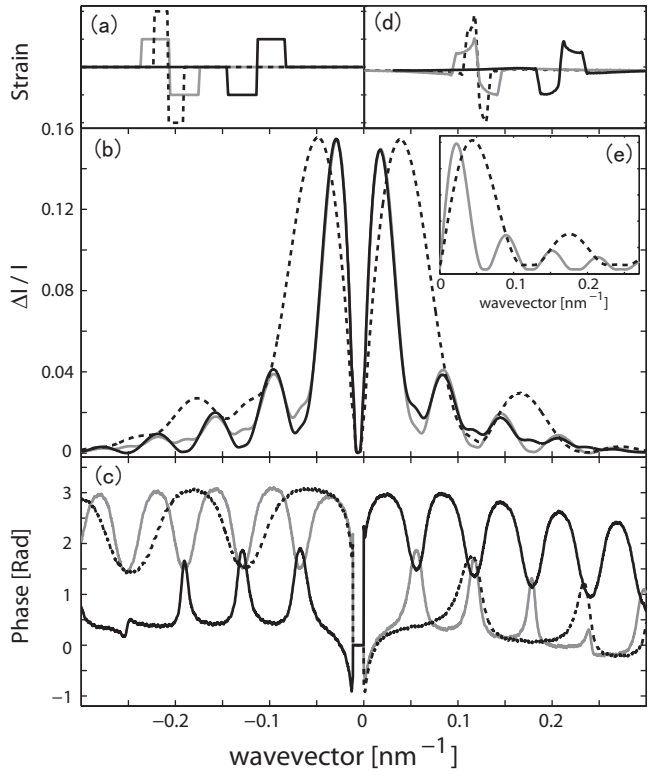

FIG. 8. (a)Simulated strain profiles for 50 nm (dashed), 100 nm (gray) and "negative" 100 nm (black) strain pulse. (b) Spectral amplitude from direct Fourier transform of the strains. (c) Retrieved spectral amplitude and (d) retrieved initial phase of the oscillation from a simulated TRXRD pattern. The amplitude is normalized to the intensity of diffraction peak. (e) Reconstructed strains from (c) and (d).

comparison, each of the pulse trains had equivalent energy. The π phase shift on either side of the diffraction angle represents the fact that the compression ($\frac{\Delta\theta_B}{\theta_o} > 0$) and rarefaction ($\frac{\Delta\theta_B}{\theta_o} < 0$) inside the crystal temporally separated. In addition, the positive slope in the angle dependent phase on the compression side of the Bragg peak reveals that the compression side of the acoustic pulse leads the rarefaction. This can be demonstrated by simulating the inverse phonon pulse. Under these circumstances the temporal phase of the acoustic wave-vectors are flipped (see figure 8).

The simulated spectral phase and amplitude demonstrates the potential power of TRXRD to differentiate between different acoustic strain waves. In particular, the addition of the static heated layer in the Thomsen strain, produces a distinct asymmetry in the spectral amplitude as well as spectral phase due to the added interference between heated surface and the generated sidebands. In addition, the square pulse and phonon pulse show distinct differences in their amplitude profile, with the square pulse possessing a higher proportion of high wave vector components.

In Figure 8, two square waves with different longitu-

dinal scale were simulated: 50 nm and 100 nm. To ensure the strains contain equivalent energy, the amplitude of acoustic pulses were adjusted. A Fourier transform of the differing strain profiles directly demonstrates the differences in high wave vector components. By simply summing all the acoustic modes together, we can roughly retrieve the spatio-temporal shape of the acoustic strain (see figure 8(e)). In particular, the reconstruction correctly orients the order of the strain pulse as well as correctly reproducing the relative spatial extent of the acoustic pulses. However there are differences in the retrieved shapes, that demonstrate the inherent limitations of TRXRD experiments. These differences between the reconstructed strain profile and the actual profile are associated with the natural resolution of the TRXRD experimental technique and will be discussed in the following section.

IV. REAL-WORLD LIMITS OF TRXRD

Provided that an x-ray pulse is not bound by the transform limit (ie. $\Delta\nu\Delta t = 0$), the analytical formalism provided above indicates that a TRXRD pattern can be inverted to reconstruct an acoustic pulse by directly measuring the amplitude and phase of the Fourier components of the strain. However, in realistic experimental conditions, the reconstruction of the transient acoustic pulse is limited by several factors including; 1. the crystal thickness, 2. finite x-ray monochromaticity, 3. the finite temporal resolution, 4. spatial divergence of the x-ray pulse, and 5. the non-zero attenuation of the x-ray pulse in the sample.

The crystal thickness physically limits the number of discrete acoustic modes that can be excited. In particular, the physical number of acoustic modes in crystalline systems are dictated by the lattice spacing and the crystal thickness. For example, in a 100 micron thick silicon (111) crystal with lattice planes separated by 3.135 Å, results in q_{max} ∼0.3 Å^{-1} and $q_{min} \sim 10^{-6}$ Å^{-1}, resulting in $\sim 10^5$ possible spatial modes.. However, as the x-ray absorption/extinction depth is often much shorter than the crystal thickness, the measurable number of acoustic modes will be limited by the x-ray interaction length ($\sim 1 - 100$ μm). As the x-ray penetration depth is often fairly deep compared to the spatial extent of the strain pulse, this constraint typically does not significantly limit the analytical power of TRXRD.

The finite x-ray monochromicity and temporal resolution are related issues, but they manifest themselves in different ways. Experimentally, the x-ray pulse has an energy bandwidth which are related to the x-ray source and any x-ray optics that are used. For example, laser based x-ray sources utilize x-ray line emission, where the central frequencies are ∼5-20 keV and have natural line widths of ∼1.5 eV[39,40] providing a natural energy resolution of $\frac{\Delta E}{E} < 10^{-3}$. Synchrotron based hard x-ray sources typically utilize a double crystal monochrometer to select the radiation[41], providing an energy resolution of $\frac{\Delta E}{E} \sim 10^{-4}$. This frequency resolution limits the ability to detect differences in acoustic modes. In particular, the measurement uncertainty of a lattice spacing due to an incoming energy bandwidth is directly related[30]:

$$\Delta d = \frac{\Delta\theta}{\theta}\frac{\Delta E}{E}\tan\theta_b \tag{11}$$

For many low order diffraction planes, this relationship indicates that acoustic modes separated by $<10^{-4}$ $\mathring{A}^{-1}$ cannot be uniquely resolved. Under realistic experimental conditions, the maximum photo-generated acoustic wave-vectors lie between $q_{max} \sim 10^{-4} - 10^{-2}$ $\mathring{A}^{-1}$, depending on the optical absorption depth and electron dynamics of the system[10]. Coupling this fact with the experimental x-ray bandwidth, the number of unique measurable acoustic modes is then limited to ∼2-100. In cases with a small number of measurable acoustic modes, the number of possible acoustic pulse shapes which can be identified is very large making a unique reconstruction challenging. For example in the work by Rose-Petruck *et al.* the optical penetration depth within the laser-excited GaAs provided a wide range of possible acoustic pulse shapes to be retrieved from the TRXRD measurement making it difficult to directly compare theoretical strain mechanisms with the experimental results[12].

The finite temporal resolution in TRXRD experiments can be due to several factors, including source size, x-ray detectors, and laser-x-ray synchronization. For example, laser based sources have been shown to have a minimum x-ray pulse widths on order of 150 fs[3], limited by the laser induced electron dynamics, while the temporal resolution of synchrotron sources are typically dictated by either ultrafast x-ray streak cameras[42,43] or the accelerated electron bunches[44–48] (∼100 fs). (Although x-ray free electron lasers have trains of attosecond x-ray pulses[49], a simple method of isolating a single attosecond pulse will be technically challenging). The temporal resolution causes an uncertainty in the phase reconstruction, through an uncertainty in zero time delay as well as a maximum frequency which can be uniquely resolved (i.e. the Nyquist frequency). For most longitudinal strains, an 100 fs x-ray pulse is much faster than any motion in the system providing ample temporal resolution to visualize the strain, however, the finite time resolution will produce a significant phase uncertainty for the high vibrational modes. In particular, the phase uncertainty will be equal to:

$$\Delta\phi = \omega_q\Delta t \tag{12}$$

where ω_q is the frequency of a particular acoustic mode and Δt is the temporal resolution of the experiment. For acoustic phonons in the linear dispersion regime, combining equation 12 with equation 6 reveals a maximum diffraction angle that can resolve the oscillation of the coherent phonon:

$$\Delta\theta = \frac{2\pi}{v_s|G|\Delta t}\tan\theta_b \tag{13}$$

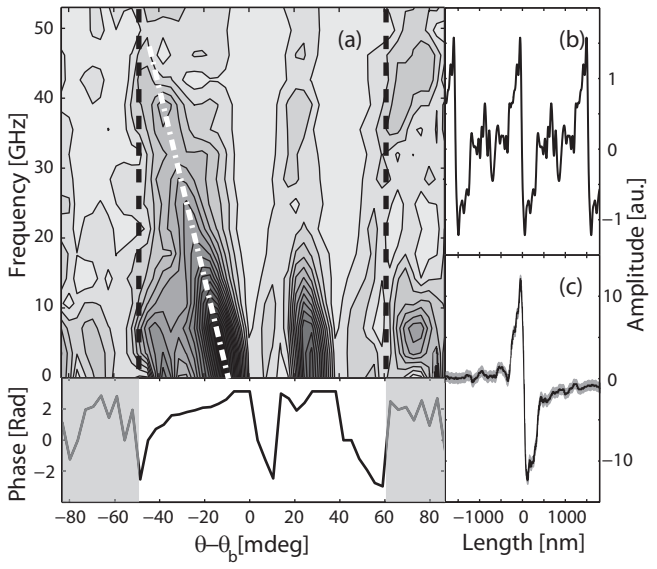

FIG. 9. Spectral amplitude and phase of sidebands retrieved form the TRXRD patterns observed for the 50 nm thick gold film. Dashed line is a guide to the eye. (b) The reconstructed spatial profile of the acoustic pulse using the data as shown. (c) The reconstructed spatial profile of the acoustic pulse obtained by adding 9 interpolated points for each data point. The shadow represents the error of reconstruction.

In figure 7 the error bars demonstrate the initial phase retrieval error due to the real-world experimental constraints. This phenomena was explicitly seen in the work by Reis *et al.*, whereby a 100 ps x-ray pulse resolved the relatively low frequency oscillating sidebands at the expense of the high wave-vector components[18]. However, simple assumptions on the spectral phase can provide intuition on the shape of the acoustic pulse. For example, for acoustic pulses generated via ultrafast laser excitation, one often assumes that the laser pulse can be treated as an instantaneous impulse to the crystalline lattice and thus all acoustic modes are excited simultaneously with the same phase. Therefore, measuring the spectral power distribution and the phase of a select number of modes, one can reconstruct the acoustic pulse with some accuracy.

V. STRAIN RECONSTRUCTION

In figure 9, we show the retrieved spectral amplitude and phase for each of the diffraction angles measured in the TRXRD pattern shown in figure 4. The Fourier transform makes it clear that the angular shift of sideband is proportional to the oscillating frequency, consistent with the acoustic dispersion relationship. Meanwhile, there is an obvious π phase shift between the negative and positive sidebands, which is consistent with the simulation above. Looking at the retrieved spectral amplitude from the Fourier transform, there is a clear asymmetry to the spectra of the positive and negative wave-vectors. This asymmetry is likely due to a slight 'static' temperature rise of the Ge substrate (<10 K), which shifts the whole rocking curve to smaller diffraction angles and increasing the observed amplitude of the oscillations.

The ultimate retrieval of the spatio-temporal strain profile is limited by the angular resolution of our setup. This constraint ultimately limits the number of unique measurable acoustic modes to ∼10, making the reconstruction process challenging. In particular, in figure 9b we numerically reconstruct the strain profile by performing a Fourier sum of the amplitude and phase retrieved from the negative sidebands for the 50 nm gold coated sample. To reconstruct the acoustic strain, we only consider the data for $\Delta T > 0$. With our experimentally limited number of modes, we see a series of strain pulses at a characteristic period associated with the inverse of the angular step size of our experiment. Even with this limitation, we can retrieve some insight into the spatio-temporal profile of the acoustic pulse. For example, we observe that the pulse is bipolar with a very rapid change in sign (<50 nm) consistent with the observed coherent sideband generation.

However, what is somewhat surprising in the Fourier reconstruction, is the spatial extent of the acoustic pulse. It has been widely assumed that the spatial extent of the generated acoustic pulse will have a scale that is approximately the twice the thickness of the metallic film[10]. However, we find that the acoustic pulse has a spatial extent of greater than 500 nm, an order of magnitude larger than the gold film thickness. This extended spatial extent can be more clearly seen if we make some simple assumptions. In particular, if we assume the amplitude and phase are smoothly varying functions such that we can perform a simple data interpolation between measured data points to artificially enhance the angular resolution to the experiment. In figure 9c, we perform a simple nine point interpolation on the data prior to Fourier reconstruction. After reconstruction, we now find that the data reveals an isolated bipolar acoustic pulse, with a sign change of less than 50 nm and a spatial extent of over >500 nm (see figure 9c). To estimate the error of our numerical reconstruction, we made a series of acoustic pulse reconstructions by assuming the measured spectral amplitude had a ∼ 20% error and a phase error dictated by temporal step-size of measurement. The resulting error in the reconstruction is shown in by the shading in figure 9c. While the phase and amplitude errors become significant for the high frequency components of the acoustic pulse, the pulse shape is dominated by the lower frequency components that are less susceptible to the phase and amplitude errors, resulting in similar retrieved pulses for all reconstructions.

The observation of this spatio-temporal elongation has not been reported in most time-domain optical[8–10,13] or TRXRD studies[16,24]. Part of this spatial dilation is likely due to the sound speed difference in gold (∼3300 m/s)

versus germanium (∼5400 m/s), which results in spatially stretching the acoustic pulse by almost a factor of two. However, the majority of this spatial elongation cannot be simply attributed to the acoustic mismatch of the materials. This result maybe due to ultrafast electron-phonon dynamics within the gold film. In particular, Wright observed that under intense ultrafast optical excitation, the non-instantaneous decay of the hot electrons will create an extended phonon pulse within the gold film[50]. If we assume that the electron phonon coupling time is 5 ps[16] this increases the effective film thickness to 65nm. Coupling this effect with the change in acoustic velocities at the gold/Ge interface, will generate a longitudinal acoustic pulse that is $\sim$ 250nm wide. The final discrepancy between the time-domain optical and TRXRD measurements may be due to a slight enhancement of the low frequency modes from the residual $< 10K$ surface heating of the crystalline substrate and/or a difference in the electron-phonon coupling time than was previously reported[16].

VI. CONCLUSION

In this paper we have measured the TRXRD patterns of photo excited gold films on a germanium crystalline substrate. These measurements demonstrate that the resulting generated acoustic pulse is bipolar with acoustic wave vectors that are determined by the metallic film thickness. In addition we have shown that there is a one-to-one correspondence between longitudinal strain pulses and a corresponding TRXRD pattern, however real world constraints limit this inversion. Even with these constraints, we are able to reconstruct the spatio-temporal shape of the impulsive generated acoustic pulse that propagates into the crystalline bulk.

We would like to thank Yi Ji, Xin Fan, Jing Qu and Lulu Zhang for technical assistance and Karl Unruh for stimulating discussions. This work is supported from the University of Delaware Research Foundation, DOE-EPSCoR grant DE-FG02-11ER46816, Army Research Office under Award No. W911NF-09-1-0390, and National Science Foundation under Award No. 0757953.

[1] A. Lindenberg *et al.*, Phys. Rev. Lett. **84**, 111 (2000).
[2] A. Cavalleri, C. Siders, C. Rose-Petruck, R. Jimenez, C. Toth, J. Squier, C. Barty, K. Wilson, K. Sokolowski-Tinten, M. von Hoegen, and D. von der Linde, Physical Review B **6319**, 193306 (2001).
[3] K. Sokolowski-Tinten and D. von der Linde, Journal of Physics-Condensed Matter **16**, R1517 (2004).
[4] A. Cavalleri, H. Chong, S. Fourmaux, T. Glover, P. Heimann, J. Kieffer, B. Mun, H. Padmore, and R. Schoenlein, Physical Review B **69** (2004).
[5] F. Schotte, M. Lim, T. Jackson, A. Smirnov, J. Soman, J. Olson, G. Phillips, M. Wulff, and P. Anfinrud, Science **300**, 1944 (2003).
[6] F. Schotte, P. Anfinrud, G. Hummer, and M. Wulff, Biophysical Journal **86**, 525A (2004).
[7] H. Maris, Scientific American **278**, 86 (1998).
[8] B. Daly, N. Holme, T. Buma, C. Branciard, T. Norris, S. Pau, D. Tennant, J. Taylor, and J. Bower, Applied Physics Letters **84**, 5180 (2004).
[9] C. Thomsen *et al.*, Phys. Rev. Lett. **53**, 989 (1984).
[10] C. Thomsen *et al.*, Phys. Rev. B **34**, 4129 (1986).
[11] J. Wark, R. Whitlock, A. Hauer, J. Swain, and P. Solone, Phys. Rev. B **35**, 9391 (1987).
[12] C. Rose-Petruck *et al.*, Nature **398**, 310 (1999).
[13] H. Y. Hao and H. Maris, Phys Rev B **64**, 064302 (2001).
[14] G. Antonelli, P. Zannitto, and H. Maris, Physica B **316-317**, 377 (2002).
[15] M. F. DeCamp, D. A. Reis, A. Cavalieri, P. H. Bucksbaum, R. Clarke, R. Merlin, E. M. Dufresne, D. A. Arms, A. M. Lindenberg, A. G. MacPhee, Z. Chang, B. Lings, J. S. Wark, and S. Fahy, Physical Review Letters **91**, 165502 (2003).
[16] M. Nicoul, U. Shymanovich, A. Tarasevitch, D. von der Linde, and K. Sokolowski-Tinten, Appl. Phys. Lett. **98**, 191902 (2011).
[17] P. Chen, I. V. Tomov, and P. M. Rentzepis, J. Chem. Phys. **104**, 10001 (1996).
[18] D. A. Reis, M. F. DeCamp, P. H. Bucksbaum, R. Clarke, E. M. Dufresne, M. Hertlein, R. Merlin, R. Falcone, H. Kapteyn, M. Murnane, J. Larsson, T. Missalla, and J. S. Wark, Phys. Rev. Lett. **86**, 3072 (2001).
[19] J. Wark, A. Allen, P. Ansbro, P. Bucksbaum, Z. Chang, M. F. DeCamp, R. Falcone, P. Heimann, S. Johnson, I. Kang, H. Kapteyn, J. Larsson, R. Lee, A. Lindenberg, R. Merlin, T. Missalla, G. Naylor, H. Padmore, D. Reis, K. Scheidt, A. Sjoegren, P. Sondhauss, and M. Wulff, Proceedings of the SPIE **4143**, 26 (2001).
[20] K. Sokolowski-Tinten *et al.*, Nature **422**, 287 (2003).
[21] M. Bargheer, N. Zhavoronkov, Y. Gritsai, J. Woo, D. Kim, M. Woerner, and T. Elsaesser, Science **306**, 5702 (2004).
[22] M. Trigo, Y. Sheu, D. A. Arms, S. Ghimire, R. Goldman, E. Landahl, R. Merlin, E. Peterson, M. Reason, and D. Reis, Phys Rev Lett **101**, 025505 (2008).
[23] K. Ichiyanagi, M. Sekiguchi, S. Nozawa, T. Sato, S. Adachi, and Y. Sasaki, Phy **84**, 024110 (2011).
[24] Y. Gao and M. F. DeCamp, Appl. Phys. Lett **100**, 191903 (2012).
[25] Y. Gao, T. Drake, Z. Chen, and M. F. DeCamp, Optics Letters **33**, 2776 (2008).
[26] S. Sayed and J. Buriak, ACS Applied Matieral Interfaces **2**, 3515 (2010).
[27] M. DeCamp, D. Reis, D. Fritz, P. Bucksbaum, E. Dufresne, and R. Clarke, Journal of Synchrotron Radiation **12**, 177 (2005).
[28] W. H. Zachariasen, *Theory of X-ray Diffraction in Crystals* (John Wiley and Sons, Inc., 1945).
[29] B. E. Warren, *X-Ray Diffraction* (Dover Publications Inc., 1990).
[30] J. Larsson, A. Allen, P. Bucksbaum, R. Falcone, A. Lindenberg, G. Naylor, T. Missalla, D. Reis, K. Scheidt, A. Sjogren, P. Sondhauss, M. Wulff, and J. Wark, Applied Physics A-Materials Science & Processing **75**, 467 (2002).
[31] C. R. Wie, T. A. Tombrello, and J. T. Vreeland, J. Appl. Phys. **59**, 3743 (1986).
[32] D. Taupin, Bull. Soc. Franç. Minér. Crist. **87**, 469 (1964).
[33] S. Takagi, Jour. Phys. Soc. Jpn. **26**, 1239 (1969).
[34] S. Takagi, Acta Cryst. **15**, 1311 (1962).
[35] F. Chukhovskii and Y. Khapachev, Physica Status Solidi A-Applied Research **88**, 69 (1985).
[36] J. Gronkowski, Physics Reports-Review Section of Physics Letters **206**, 1 (1991).
[37] S. Podorov, V. Punegov, and V. Kusikov, Phys. Solid State **36**, 454 (1994).
[38] D. Reis and A. Lindenberg, "Light scattering in solids IX," (Springer, 2007) Chap. Ultrafast X-ray scattering in solids.
[39] T. Guo, C. Spielmann, B. Walker, and C. Barty, Review of Scientific Instruments **72**, 41 (2001).
[40] Y. Jiang, T. Lee, and C. Rose-Petruck, Journal Of The Optical Society Of America B-Optical Physics **20**, 229 (2003).
[41] B. Yang and others., Nuclear Instruments and Methods in Physics Research A **316**, 422 (1992).
[42] Z. Chang, A. Rundquist, J. Zhou, M. Murnane, H. Kaptey, X. Liu, B. Shan, J. Liu, L. Niu, M. Gong, and X. Zhang, Appl. Phys. Lett **69**, 133 (1996).
[43] J. Larsson, Z. Chang, E. Judd, P. Schuck, R. Falcone, P. Heimann, H. Padmore, H. Kapteyn, P. Bucksbaum, M. Murnane, R. Lee, A. Machacek, J. Wark, X. Liu, and B. Shan, Optics Letters **22**, 1012 (1997).
[44] R. Schoenlein, W. Leemans, A. Chin, P. Volfbeyn, T. Glover, P. Balling, M. Zolotorev, K. Kim, S. Chattopadhyay, and C. Shank, Science **274**, 236 (1996).
[45] R. Schoenlein, S. Chattopadhyay, H. Chong, T. Glover, P. Heimann, W. Leemans, C. Shank, A. Zholents, and M. Zolotorev, Applied Physics B-Lasers and Optics **71**, 1 (2000).
[46] W. Leemans, R. Schoenlein, P. Volfbeyn, A. Chin, T. Glover, P. Balling, M. Zolotorev, K. Kim, S. Chattopadhyay, and C. Shank, IEEE Journal Of Quantum Electronics **33**, 1925 (1997).
[47] W. Leemans, R. Schoenlein, P. Volfbeyn, A. Chin, T. Glover, P. Balling, M. Zolotorev, K. Kim, S. Chattopadhyay, and C. Shank, Physical Review Letters **77**, 4182 (1996).
[48] R. Schoenlein, S. Chattopadhyay, H. Chong, T. Glover, P. Heimann, C. Shank, A. Zholents, and M. Zolotorev, Science **287**, 2237 (2000).
[49] H. Nuhn, Nuclear Instruments and Methods in Physics Research A **429**, 249 (1999).
[50] O. Wright, Physical Review B **49**, 9985 (1994).